ACS APPLIED MATERIALS & INTERFACES

Research Article

www.acsami.org

Metal Selenides as a New Class of Electrocatalysts for Quantum Dot-Sensitized Solar Cells: A Tale of $Cu_{1.8}Se$ and PbSe

Hye Mi Choi,[†] In Ae Ji,[†] and Jin Ho Bang*[,†,‡]

[†]Department of Bionanotechnology and [‡]Department of Chemistry and Applied Chemistry, Hanyang University, 55 Hanyangdaehak-ro, Sangnok-gu, Ansan, Kyeonggi-do 426-791, Republic of Korea

Supporting Information

ABSTRACT: The development of a Pt-free, highly active electrocatalyst for a counter electrode (CE) is vital to the construction of highly efficient quantum dot-sensitized solar cells (QDSSCs). As an alternative to Pt, the use of various metal sulfides, such as Cu_2S, CoS, and PbS, has been successfully demonstrated; however, the studies on the utilization of non-sulfide materials have been scarcely reported. In this regard, we examined eight different types of binary metal selenides as new candidate materials, and found that the electrocatalytic activity of $Cu_{1.8}Se$ and PbSe toward polysulfide reduction was superior to that of Pt. In depth investigation into these two materials further revealed that, while the electrocatalytic activity of both metal selenides surpasses that of Pt, the long-term utilization of the PbSe CE is hindered by the formation of PbO on the surface of PbSe, which is attributed to the instability of PbSe under air. Unlike PbSe, $Cu_{1.8}Se$ was found to be chemically stable with a polysulfide electrolyte and was even better than Cu_2S, a commonly used CE material for QDSSCs. Using the $Cu_{1.8}Se$ CE, we obtained a power conversion efficiency of 5.0% for CdS/CdSe-sensitized solar cells, which was an efficiency almost twice that obtained from Pt CE. This work provides a new application for metal selenides, which have been traditionally utilized as sensitizers for QDSSCs.

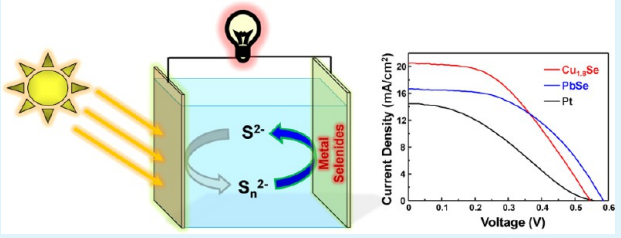

KEYWORDS: *counter electrode, metal selenides, polysulfide electrolyte, Pt corrosion, electrocatalytic activity*

1. INTRODUCTION

Quantum dot-sensitized solar cells (QDSSCs) have received great attention recently as next-generation solar cells due to the intriguing physical properties of QDs and their low-cost and simple fabrication process.[1] The basic working principle of QDSSCs is similar to that of their analogue, dye-sensitized solar cells (DSSCs). In a typical operation, photo-excited electrons are injected from sensitizers (QDs or dye molecules) into TiO_2, and the electrons flow through an external circuit to a counter electrode (CE), where oxidized redox species generated during the hole scavenging process are reduced by the electrons. Looking back on the development of DSSCs and QDSSCs, most studies have focused on the development of photoelectrodes.[2−15] However, since the efficiency of the solar cells is governed by the characteristics of both the photoelectrode and counter electrode, the development of a highly efficient electrocatalyst for the CE is extremely important. The traditional electrocatalyst for the CE of DSSCs and QDSSCs is platinum (Pt). While its high cost is a drawback, Pt still holds the unchallenged position as the best CE material for DSSCs. In the case of QDSSCs, however, Pt does not have such a unique status because it is subjected to serious corrosion when in contact with the polysulfide electrolyte, a common electrolyte for QDSSCs.[16] The poor electrocatalytic activity of Pt caused by such corrosion has long been one of the key issues in the development of highly efficient QDSSCs.[17] Various non-platinum materials have been proposed as CE materials, among which metal sulfides, such as CuS, Cu_2S, CoS, CoS_2, PbS, $CuInS_2$, and Cu_2ZnSnS_4, exhibited superior electrocatalytic activity compared with Pt.[18−26] In fact, the development of highly active electrocatalysts for CE has been a driving force for the recent dramatic increase in the efficiency of QDSSCs.

Despite the successful utilization of metal sulfide electrocatalysts, little attention has been paid to the use of metal selenides as a CE material for QDSSCs. This is partly because metal selenides have long been utilized as sensitizers for photoelectrodes. Recently, we demonstrated the first utilization of metal selenides as the electrocatalyst for polysulfide reduction.[27] Our study revealed that $Cu_2ZnSnSe_4$ could be employed as an alternative electrocatalyst for the CE of QDSSCs; however, its electrocatalytic activity was only comparable to that of Pt. Another recent report demonstrated that $Cu_2ZnSnSe_4$ nanoparticles composited with carbon nanotubes were capable of achieving a higher power conversion efficiency of 4.6%, highlighting again the feasibility of metal selenides as electrocatalysts for QDSSCs.[28] To date, no study has been reported on any metal selenide other than $Cu_2ZnSnSe_4$. In this report, therefore, we performed a systematic study on binary metal selenides to assess their

Received: October 4, 2013
Accepted: February 3, 2014
Published: February 3, 2014

feasibility as electrocatalysts and to elucidate their electrochemical behavior and influence on solar cell performance. Among the metal selenides we examined, PbSe and $Cu_{1.8}Se$ excelled in the electrocatalytic activity compared with Pt. Our in-depth investigation also revealed that unlike $Cu_{1.8}Se$, PbSe was much more vulnerable to oxidation, thus losing its electrocatalytic activity over time. The $Cu_{1.8}Se$ electrocatalyst was found to be even better than Cu_2S, the most common electrocatalyst for highly efficient QDSSCs, opening up a new possibility for metal selenides as electrocatalysts for CE in addition to their traditional role as a photoelectrode sensitizer.

2. EXPERIMENTAL SECTION

2.1. Preparation of Photoelectrodes. F-doped SnO_2 (FTO, Pilkington TEC 15, Hartford Glass, Inc.) plates were thoroughly cleaned with HCl, acetone, ethanol, and deionized water, sequentially, under sonication for 30 min each. Nanoporous oxide films for use as photoelectrodes were prepared by spin-coating TiO_2 paste onto the clean FTO plates. The TiO_2 paste was obtained by dispersing TiO_2 nanopowder (3.3 g; Degussa P-25, Evonik Industries) in mixed solvents containing 1-methoxy 2-propanol (1 mL), methanol (3 mL), ethanol (4 mL), and deionized water (2 mL) under vigorous stirring (40 min), followed by sonication (15 min). A TiO_2 layer with a thickness of ~15 μm was deposited by repeating the spin-coating process 3 times (Figure S1 in Supporting Information (SI)), and the resulting oxide films were subsequently annealed at 450 °C under air for 40 min. QD sensitizers were deposited onto TiO_2 via a successive ionic layer adsorption and reaction (SILAR) method. Prior to CdSe deposition, a co-sensitizer, CdS, was deposited. In a typical procedure, the TiO_2 films were immersed into an aqueous $Cd(NO_3)_2$ (0.1 M) solution for 3 min, and they were then rinsed with deionized water for 30 sec. After drying, they were immersed in an aqueous Na_2S (0.1 M) solution for another 3 min, followed by rinsing and drying. This procedure constituted one SILAR cycle, which was repeated 5 times. A CdSe sensitizer was deposited over the CdS/TiO_2 films in a similar fashion under an inert atmosphere.[3] $Cd(NO_3)_2$ was dissolved in ethanol (30 mM), and SeO_2 dissolved in ethanol (30 mM) was reduced with two equivalents of $NaBH_4$ until a clear, transparent solution was obtained. The SILAR for the CdSe deposition was carried out by immersing the CdS/TiO_2 films alternately into the Cd cation (Cd^{2+})-containing solution and the Se anion (Se^{2-})-containing solution for 30 s each. The films were rinsed with ethanol for 30 s between each immersion. Nine cycles of this SILAR process were performed to deposit CdSe. Finally, a ZnS passivation layer was coated over the CdSe/CdS/TiO_2 films via the SILAR process, where the films were dipped alternately in an aqueous $Zn(CH_3COO)_2$ (0.1 M) solution for 1 min and aqueous Na_2S (0.1 M) solution for 1 min, for two cycles. Figure S2 in SI shows X-ray diffraction (XRD) pattern and diffuse reflectance ultraviolet-visible (UV–vis) absorption spectrum of the CdSe/CdS/TiO_2 film. While the broad diffraction peaks from CdSe appeared along with intense peaks from TiO_2 (anatase (JCPDS 21-1272) and rutile (JCPDS 21-1276)) and from FTO (JCPDS 46-1088), they matched the peaks from wurtzite CdSe (JCPDS 19-0191). The deposition of CdSe sensitizer was also confirmed by the UV–vis absorption spectrum, where the entire visible light was absorbed by the CdSe/CdS/TiO_2 film. Figure S3 in SI displays the energy dispersive X-ray spectroscopy (EDS) elemental mapping analysis of the CdSe/CdS/TiO_2 film, showing that the CdSe/CdS layer was uniformly deposited over the entire TiO_2 film.

2.2. Preparation of Counter Electrodes. Metal selenide CEs were prepared by the SILAR process. Prior to the SILAR process, the cleaned FTO plates were pre-treated by dipping them in an aqueous KOH solution (0.5 M) for 1 h. We found that this KOH treatment was of great benefit for the uniform deposition of metal selenides on FTO, which may be attributed to the strong complexation power of hydroxide.[29] For the SILAR process, 30 mM metal chloride solutions in ethanol (for MnSe and PbSe, metal acetates were used) and SeO_2 dissolved in ethanol (30 mM) were used. For the preparation of $Cu_{1.8}Se$, Bi_2Se_3, and PbSe films, the saturated solutions of each metal salt were used because of limited solubility. SILAR was performed by immersing the KOH-treated FTO plates into the prepared solutions alternately for 30 sec under an inert atmosphere. The films were rinsed only after the FTO plates were taken out of the Se^{2-}-containing solution. SILAR was implemented by immersing the KOH-treated FTO plates into the prepared solutions alternately for 30 sec, and the SILAR cycles were repeated 12 times. For the preparation of the Cu_2S and PbS CEs, a similar SILAR process was carried out except for the use of Na_2S solution. For the fabrication of the Pt CE, Platisol S/TP (Solaronix) was deposited using a doctor-blade technique onto FTO and was then annealed at 450 °C for 30 min. The weight of electrocatalysts loaded on FTO was measured by a microbalance (A&D BM-22, readability to 1 μg).

2.3. Solar Cell Fabrication. The polysulfide electrolyte was prepared by dissolving sulfur in an aqueous Na_2S and NaOH solution (2 M S, 2 M Na_2S, and 0.1 M NaOH) under vigorous stirring. The CdSe-sensitized photoelectrodes and each CE were clamped with a Surlyn spacer (60 μm, Solaronix) in between and sealed by mild heating. The prepared polysulfide electrolyte was injected into the cell through a small hole in the CE via vacuum backfilling, and the hole was covered using Surlyn and a coverslip. For electrochemical impendence spectroscopy (EIS) and Tafel measurements, symmetric dummy cells were prepared by assembling two identical CEs face-to-face and filling the polysulfide electrolyte in the same manner.

2.4. Characterization. XRD patterns were recorded using an X-ray diffractometer (Rigaku D/Max-2500/PC). Scanning electron microscopy (SEM) was carried out using a field-emission scanning electron microscope (Hitachi S-4800 FESEM) equipped with an EDS detector. Transmission electron microscopy (TEM) was conducted using a JEOL 2010F at an acceleration voltage of 200 kV. For the TEM analysis, $Cu_{1.8}Se$ and PbSe were carefully scratched off of each electrode, dispersed in ethanol by sonication, and dropped onto TEM grids. The TEM samples were dried under vacuum before measurement. Raman spectra were obtained with a Renishaw 2000 confocal Raman microscope system. X-ray photoelectron spectroscopy (XPS) measurements were performed using a PHI Versa Probe system with a 100 W Al K Alpha X-ray source with a spot size of 400 μm at a 45° incident angle. Diffuse reflectance UV–vis absorption spectra were recorded using a UV–vis spectrophotometer (SCINCO S-3100) equipped with a diffuse reflector (SCINCO). A solar simulator (HAL-320, Asahi Spectra) was employed as a light source. The intensity of light generated from the solar simulator was adjusted to 1 SUN (Air Mass 1.5G) using a 1 SUN checker (CS-20, Asahi Spectra). Photocurrent-photovoltage (J–V) curves were recorded using a Keithley 2400 source meter under illumination. The active area of the solar cells was 0.20 cm^2, and a black mask was placed over the solar cells to prevent stray light from reaching the sample. A potentiostat (CH Instruments, CHI 660D electrochemical workstation) was employed to perform EIS and Tafel measurements. EIS spectra were measured under a frequency range of 0.1 Hz to 100 kHz and a perturbation amplitude of 10 mV, and Tafel polarization curves were obtained at a scan rate of 50 $mV \cdot s^{-1}$.

3. RESULTS AND DISCUSSION

Eight different types of binary selenides (MnSe, $CoSe_2$, $NiSe_2$, $Cu_{1.8}Se$, $MoSe_2$, WSe_2, PbSe, and Bi_2Se_3) were initially chosen as electrocatalyst candidates for CE in this study. These metal selenides were deposited directly on FTO substrates via the SILAR method. Given that many metal sulfide CEs have been prepared by immersing metal foils into a sulfide solution or by applying a paste composed of metal sulfide nanoparticles embedded on various carbons (e.g., reduced graphene oxide, carbon black, etc.) onto FTO,[18,21,22] the facile processability and reproducibility of the SILAR method is of great benefit in the search for efficient electrocatalysts from the candidate materials. Before applying the metal selenide films prepared by the SILAR method to QDSSCs as CEs, the SILAR process was

optimized to produce uniform, robust films. We particularly investigated the dependence of the electrochemical properties of the metal selenide films on the SILAR cycles. As a representative example, the investigation into the PbSe film is presented; it is important to note that all other metal selenide films exhibited a similar trend.

Figure S4A in SI shows the diffuse-reflectance UV−vis absorption spectra of PbSe films, in which the absorbance gradually increased with the SILAR cycles, indicating that the PbSe films became thicker. The SEM analysis of the films also revealed that the FTO substrates were not fully covered with PbSe nanoparticles when 4 cycles of SILAR were performed (SI Figure S5). When the SILAR process was repeated 8 times, the coverage of PbSe was significantly improved, but the PbSe film showed a lack of uniformity. In our study, 12 cycles of SILAR yielded a fairly uniform PbSe film. We speculated that such a variation in the coverage may have a considerable influence on the electrochemical properties of the PbSe films because the degree of coverage is intimately associated with active surface area and conductivity of the film.[21,30,31] To investigate the electrocatalytic activity of PbSe films in the polysulfide electrolyte, Tafel polarization curves were obtained using symmetric dummy cells composed of two identical PbSe films with the polysulfide electrolyte (2 M S, 2 M Na_2S, and 0.1 M NaOH) in between them. The Tafel polarization curve measurement is a simple, powerful tool for the evaluation of the electrocatalytic activity of CE materials because the exchange current (i_0), which reflects the electrocatalytic activity, can be easily estimated from the extrapolated intercepts of the anodic and cathodic branches of the Tafel polarization curves. i_0 is described in eq 1

$$i_0 = \frac{RT}{nFR_{ct}} \quad (1)$$

where R is the gas constant, T is the absolute temperature, n is the number of electrons involved in the polysulfide reduction, F is the Faraday constant, and R_{ct} is the charge-transfer resistance. SI Figure S4B shows that the anodic and cathodic branches of the Tafel curve moved upward as the SILAR cycles increased, implying that the electrocatalytic activity of the PbSe films substantially improved as they became thicker and more uniform. The PbSe film obtained after only 4 cycles of SILAR exhibited a much lower i_0, which resulted from an incomplete coverage of PbSe (i.e., not many catalytically active sites). While the larger active surface area of the PbSe film obtained after the 8 cycles of SILAR was capable of enhancing i_0, the non-uniformity of the PbSe layer gave rise to a poor connection between the PbSe nanoparticles, preventing efficient electron transport through the nanoparticle network. The enhanced electrocatalytic activity of the PbSe film obtained after the 12 cycles of SILAR is therefore attributed to a larger active surface area and an improved connection between PbSe nanoparticles.[32] To further support our claim, EIS measurements were carried out with the symmetric dummy cells. Nyquist plots and an equivalent circuit, from which EIS parameters are extracted, are presented in SI Figures S4C and S4D. The EIS parameters are summarized in SI Table S1. SI Figure S4C shows that the semi-circles in the Nyquist plots became smaller as the SILAR cycles increased, which is indicative of a decrease in charge transfer resistance with increasing SILAR cycles. This is consistent with the trend observed in the Tafel polarization curves.

The metal selenide films deposited on FTO substrate by the 12 cycles of SILAR were utilized as CEs for QDSSC, and their solar cell performance was compared with that of a QDSSC fabricated with a Pt CE. Figure 1 displays the current-voltage

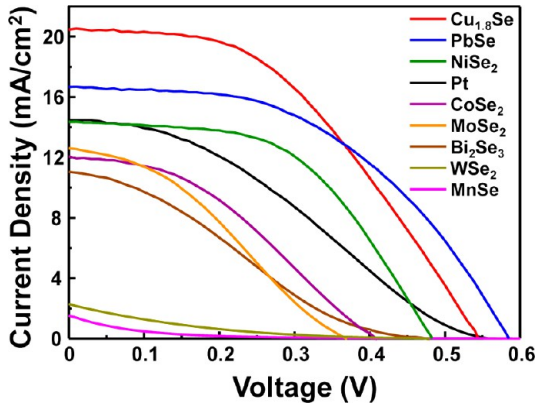

Figure 1. $J-V$ curves of QDSSCs with various metal selenide CEs under 1 SUN (Air Mass 1.5G) illumination.

($J-V$) curves of the QDSSCs, and the solar cell parameters, such as short-circuit current (J_{sc}), open-circuit voltage (V_{oc}), fill factor (FF), and power conversion efficiency (η), are summarized in Table 1. Only the QDSSCs made with

Table 1. Solar Cell Parameters of QDSSCs with Various Metal Selenide CEs

counter electrode	J_{sc} (mA/cm^2)	V_{oc} (V)	FF	η (%)
$Cu_{1.8}Se$	20.5	0.54	0.50	5.01
PbSe	16.7	0.59	0.48	4.71
$NiSe_2$	14.3	0.48	0.52	3.63
Pt	14.5	0.56	0.33	2.66
$CoSe_2$	12.1	0.41	0.38	1.85
$MoSe_2$	12.6	0.37	0.34	1.57
Bi_2Se_3	11.0	0.48	0.26	1.4
WSe_2	2.3	0.47	0.13	0.14
MnSe	1.52	0.51	0.06	0.05

$Cu_{1.8}Se$, PbSe, and $NiSe_2$ CEs showed better performances than that with Pt. When the other CEs were employed, the solar cell performance was inferior. The poor performance of the CEs except for $Cu_{1.8}Se$, PbSe, and $NiSe_2$ CEs is well-supported by the Tafel polarization curves and EIS results in SI Figure S6 and S7 and SI Table S2. While the QDSSC made with $NiSe_2$ CE exhibited a better power conversion efficiency than that made with Pt, its J_{sc} and V_{oc} were in fact worse than those obtained from the Pt CE-employed QDSSC. The improvement in performance originated from the significant increase in FF. On the basis of our preliminary results, we decided to perform an in-depth study on only $Cu_{1.8}Se$ and PbSe, both of which showed result superior to Pt in all of the solar cell parameters.

Figure 2A shows the XRD patterns of $Cu_{1.8}Se$ and PbSe films deposited on FTO substrate. In the case of $Cu_{1.8}Se$, all the diffraction peaks are indexed to cubic phase $Cu_{1.8}Se$ (JCPDS 65-2982) except the signals from the FTO substrate. In the case of PbSe, however, there were minor peaks from PbO (JCPDS 65-0401) observed along with the peaks from cubic phase PbSe (JCPDS 65-2941). Because of the small crystal sizes in each film, all the diffraction peaks were broad, so that the detection

dx.doi.org/10.1021/am404355m | ACS Appl. Mater. Interfaces 2014, 6, 2335−2343

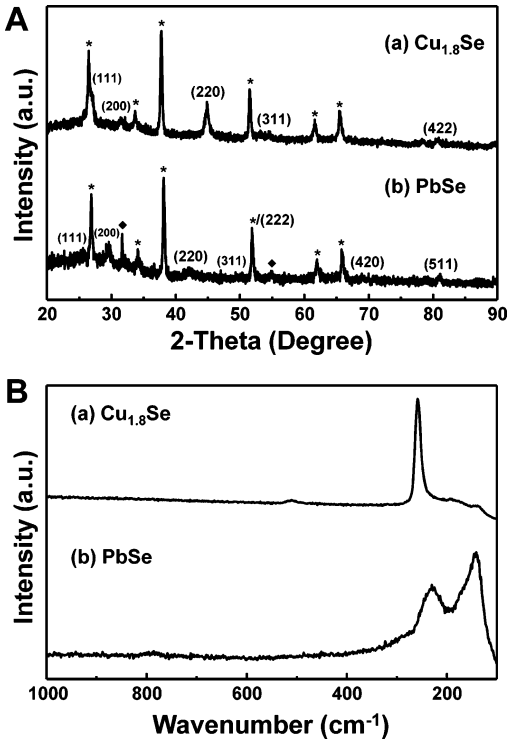

Figure 2. (A) XRD patterns of (a) $Cu_{1.8}Se$ and (b) PbSe films (peaks from FTO substrate and PbO are marked with asterisks and diamonds, respectively). (B) Raman spectra of (a) $Cu_{1.8}Se$ and (b) PbSe films.

of minor crystal phases by XRD was a bit ambiguous. To affirm the XRD result, we conducted Raman spectroscopy because of its capability to monitor average crystal structure over a large area.[33] The Raman spectrum of the $Cu_{1.8}Se$ film (Figure 2B) displayed a strong, sharp peak at 258 cm^{-1}, which matched the known $Cu_{1.8}Se$ Raman peak well. The Raman mode at this wavenumber corresponded to the Se−Se stretch vibration of Se^{2-} ions and was assigned to the A_{1g} mode.[34] A weak, broad band at 513 cm^{-1} resulted from the first overtone of the strongest peak in the spectrum. The Raman spectrum of PbSe, on the other hand, shows two distinct peaks at 142 and 230 cm^{-1} (Figure 2B), which are attributed to the longitudinal optical phonon of PbSe and to selenium, which may be segregated from Pb^{2+} because of the formation of PbO, respectively.[35] The Raman analysis of the PbSe film is in accordance with the result obtained by the XRD analysis, confirming that the PbSe film was partly oxidized.

XPS analysis was also performed on both films to investigate their surface oxidation states and chemical compositions (see the survey spectra in SI Figure S8). Figures 3A and 3B show the Cu 2p and Se 3d spectra obtained from the $Cu_{1.8}Se$ film. The Cu $2p_{3/2}$ and Cu $2p_{1/2}$ peaks at the binding energies of 932.0 and 951.8 eV were deconvoluted into three peaks that were from Cu^{2+}, Cu^{+}, and shake-up satellites due to the presence of paramagnetic Cu^{+} species. The Se $3d_{5/2}$ and $3d_{3/2}$ peaks appeared at the binding energies of 53.4 and 53.9 eV, which were attributed to Se^{2-} in $Cu_{1.8}Se$, and no selenium oxide species were found. The XPS result implied the relatively good air-stability of $Cu_{1.8}Se$ in contrast to Cu_2Se, which is known to be unstable under air.[36] The XPS quantitative analysis confirmed that the chemical composition of Cu:Se was 1.8:1, which is in good agreement with the XRD and Raman results. Figures 3C and 3D show the Pb 4f and Se 3d spectra obtained from the PbSe film. Along with the Pb $4f_{7/2}$ and $4f_{5/2}$ peaks at

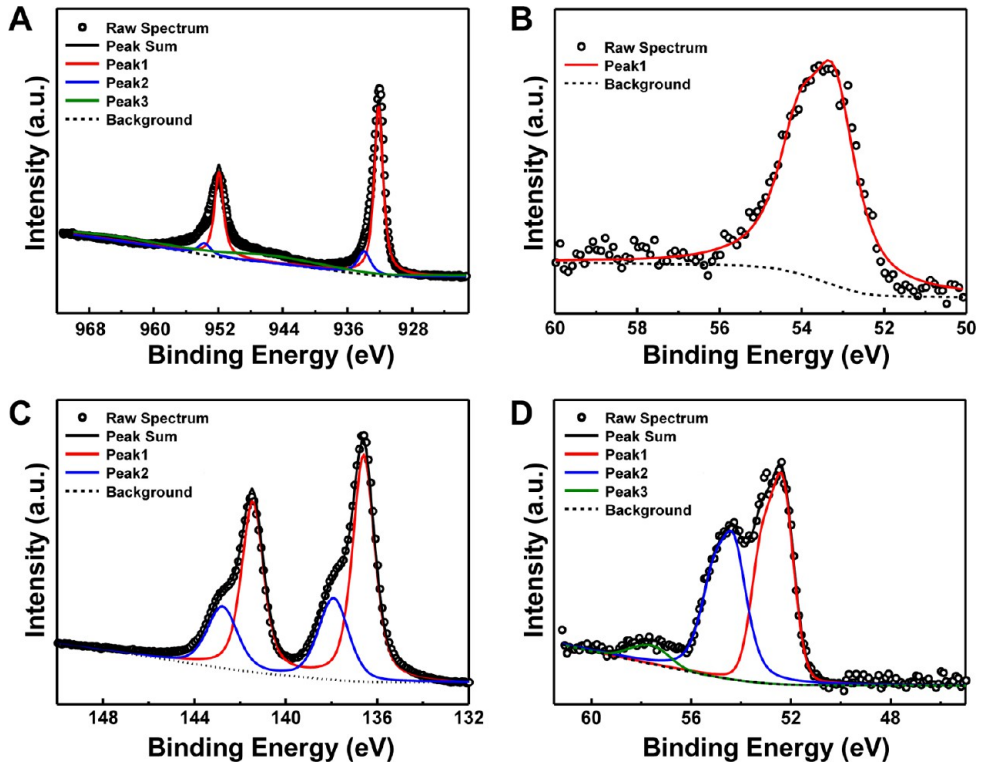

Figure 3. XPS spectra of (A) Cu 2p (peak 1, Cu^{+} from $Cu_{1.8}Se$; peak 2, Cu^{2+} from $Cu_{1.8}Se$; peak 3, shake-up satellites due to Cu^{+}), (B) Se 3d from the $Cu_{1.8}Se$ film, (C) Pb 4f (peak 1, Pb^{2+} from PbSe; peak 2, Pb^{2+} from PbO), and (D) Se 3d (peak 1, Se^{2-} from PbSe; peak 2, intermediate oxidation state (roughly corresponding to Se^{0}); peak 3, Se^{4+} from SeO_2) from the PbSe film.

dx.doi.org/10.1021/am404355m | ACS Appl. Mater. Interfaces 2014, 6, 2335−2343

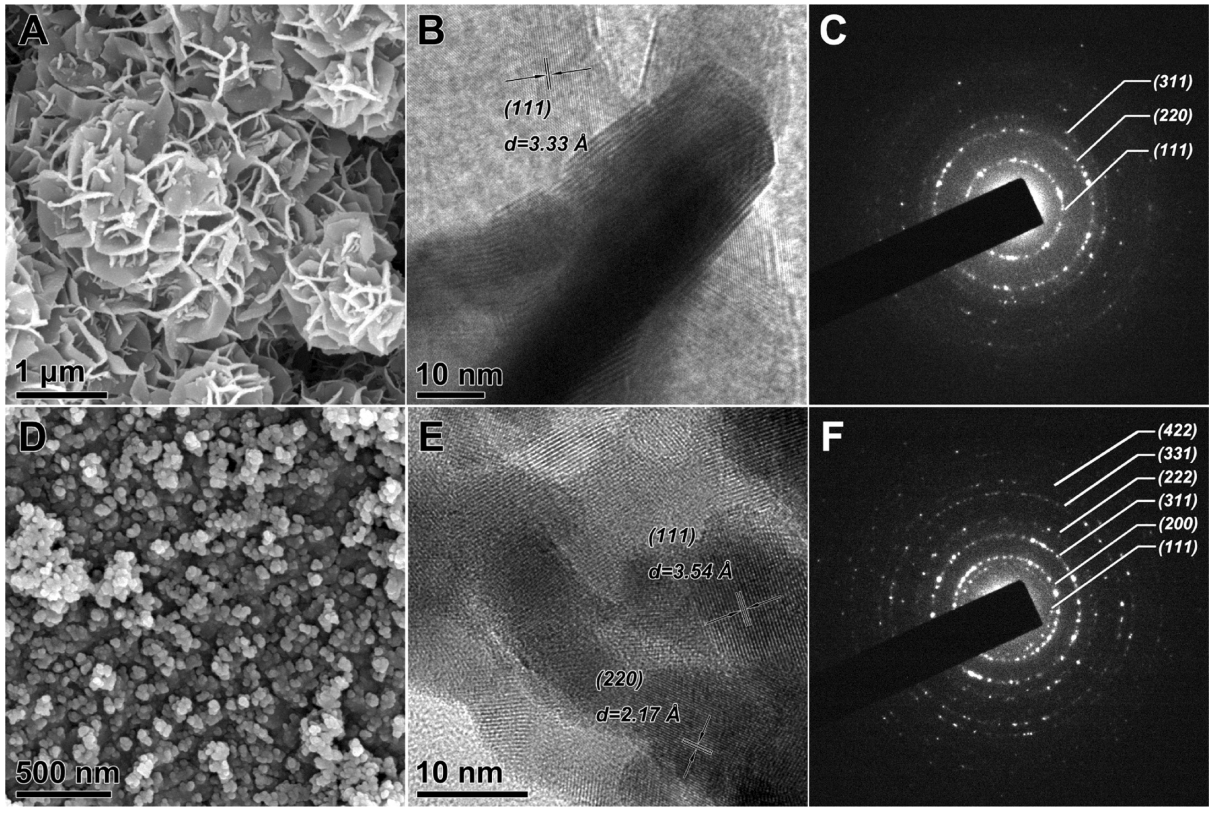

Figure 4. (A) SEM image, (B) TEM image, and (C) SAED of the $Cu_{1.8}Se$ film; (D) SEM image, (E) TEM image, and (F) SAED of the PbSe film.

the binding energies of 136.6 and 141.5 eV from Pb^{2+} in PbSe, shoulders on the high binding energy side were observed in the Pb 4f spectrum, which were ascribed to Pb^{2+} in PbO. Unlike the Se spectrum obtained from the $Cu_{1.8}Se$ film, the Se 3d spectrum obtained from the PbSe film exhibited three peaks, which were deconvoluted into Se^{2-} from PbSe, intermediate Se species, and Se^{4+} from SeO_2. The XPS analysis revealed that PbSe was partly oxidized to PbO and SeO_2 due to its instability under air, which is in good accordance with the XRD and Raman results.

The morphology and crystal structure of both films were investigated using electron microscopy. Figure 4 shows the SEM and TEM images of $Cu_{1.8}Se$ and PbSe films along with their selected area electron diffraction (SAED) patterns (see the low magnification SEM image in SI Figure S9). The SEM images (Figures 4A and 4C) showed that myriad nanoflakes were assembled into a flower-like nanostructure in the $Cu_{1.8}Se$ film, whereas spherical nanoparticles of 40−50 nm were compactly deposited onto FTO in the PbSe film. The thickness of $Cu_{1.8}Se$ and PbSe films was determined to be 6.6 and 1.4 μm, respectively, by the SEM analysis (SI Figure S10), and we observed that SILAR method yielded fairly uniform and reproducible films. The TEM images in Figures 4B and 4E show a lattice fringe of $Cu_{1.8}Se$ with an inter-spacing of 3.33 Å corresponding to the (111) crystal plane and those of PbSe with inter-spacings of 3.54 and 2.17 Å corresponding to the (111) and (220) crystal planes, respectively. The SAED patterns shown in Figures 4C and 4F divulged the polycrystalline nature of both films.

The performance of the QDSSCs with the $Cu_{1.8}Se$ and PbSe CEs was superior to that of the QDSSC with the Pt CE due to significantly improved J_{sc} and FF (Table 1). Such improvements result from the high electrocatalytic activity of these novel CEs toward the polysulfide reduction (S_n^{2-} + 2e → S_{n-1}^{2-} + S^{2-}). To affirm our claim, the electrochemical properties of $Cu_{1.8}Se$ and PbSe films were investigated using Tafel polarization curves and EIS measurements. Note that the absolute loading masses of $Cu_{1.8}Se$ and PbSe on FTO were almost identical (0.940 and 0.934 mg for $Cu_{1.8}Se$ and PbSe), so that the difference in electrocatalytic activity of these two metal selenides solely originated from their own electrocatalytic activity. The thickness of Pt film was determined to be ∼800 nm with a Pt loading of 5.295 mg (SI Figure S11), which was 5 times higher amount than those of $Cu_{1.8}Se$ and PbSe. Tafel polarization curves from the $Cu_{1.8}Se$, PbSe, and Pt electrodes are compared in Figure 5A, revealing that i_0 values of both $Cu_{1.8}Se$ and PbSe electrodes were greater than that of Pt by more than two orders of magnitude. The $Cu_{1.8}Se$ electrode showed a higher i_0 than the PbSe electrode, which reflects the solar cell performance shown in Figure 1. A slight deviation from the equilibrium potential was noticed in the Pt electrode, which may be ascribed to the adsorption of sulfur species in the electrolyte onto the surface of Pt, as noted in a previous report.[30] EIS measurements were executed to investigate the charge transfer resistances, and the resulting Nyquist plots are shown in Figure 5B (the entire Nyquist plot of Pt CE is provided in SI Figure S12). The EIS parameters extracted from the equivalent circuit in Figure 5C are summarized in Table 2. In the Nyquist plots, the high-frequency intercepts are related to sheet resistances, the first high-frequency arches arise from the solid−solid interface, and the second semi-circles are associated with charge transfer process occurred at the CE-electrolyte interface.[21,37] The sheet resistances, represented by R_1, are similar for all CEs, and the resistances caused by the solid−solid interface (R_2) in each film are not significantly different. The Pt CE demonstrated the smallest R_2 and the

dx.doi.org/10.1021/am404355m | ACS Appl. Mater. Interfaces 2014, 6, 2335−2343

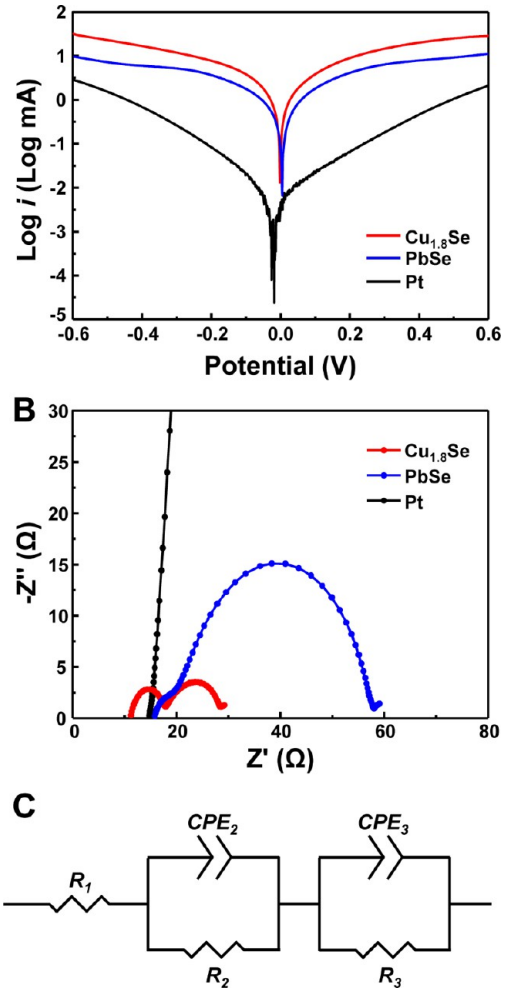

Figure 5. (A) Tafel polarization curves, (B) EIS spectra of Pt, $Cu_{1.8}Se$, and PbSe electrodes, and (C) an equivalent circuit employed to fit the EIS spectra (R_1 = ohmic serial resistance, R_2 = charge-transfer resistance of solid/solid interface, R_3 = charge-transfer resistance of electrolyte/CE interface, CPE_2 = constant phase angle element of solid/solid interface, and CPE_3 = constant phase angle element of electrolyte/CE interface).

PbSe CE demonstrated the highest R_2, revealing the order of electrical conductivity among the CEs. Notably, the $Cu_{1.8}Se$ CE possessed less resistance than the PbSe CE, reflecting the superior electrical conductivity of $Cu_{1.8}Se$.[36] Given that the sums of R_1 and R_2 of each CE are similar, it is reasonable to claim that the difference in the electrocatalytic activity of each CE is intimately associated with the charge transfer resistance (R_3), which mainly dictates the electrocatalytic activity of CE materials. Figure 5B shows that the radius of the second semicircle of the $Cu_{1.8}Se$ CE is smaller than that of the PbSe CE, which is indicative of a smaller R_3 (that is, a faster electron transfer rate). The R_3 values were found to be 7464, 13.4, and 36.3 Ω for Pt, $Cu_{1.8}Se$, and PbSe CEs, respectively (Table 2), which is consistent with the trend observed in the Tafel polarization curves. To cross-check the validity of the R_3 values, we calculated the i_0 values of Pt, $Cu_{1.8}Se$, and PbSe CEs (1.72, 958, and 353 mA, respectively) using eq 1 with the obtained R_3, and found that they closely match i_0 of each CE obtained from the Tafel curve measurements (3.31, 994, and 366 mA, respectively). In addition to a smaller R_3, the $Cu_{1.8}Se$ CE showed a smaller α and a higher constant phase element (CPE_3) than the PbSe CE, where interfacial capacitance is described as $Z_{CPE} = A(jw)^{-\alpha}$ ($0 \leq \alpha \leq 1$), where w is the angular frequency and A and α are frequency-independent parameters (Table 2). It is known that the CPE values can reflect the roughness of electrodes and the degree of deviation of α from 1 can be related to the porosity of the electrodes.[37,38] The smaller α and higher CPE_3 determined for the $Cu_{1.8}Se$ CE may therefore suggest that the $Cu_{1.8}Se$ CE has a larger surface area for more electrocatalytic sites and larger porosity for the efficient diffusion of polysulfide electrolyte as compared to the PbSe CE. This analysis is in line with the difference in morphology observed in our SEM analysis, where a porous, flower-like nanostructure was observed in the case of the $Cu_{1.8}Se$ CE, whereas a compact film composed of nanoparticles in the case of the PbSe CE. We speculate that this morphological difference may also contribute to the difference in the electrocatalytic activity along with the disparity in the charge transfer rate.

While the improved QDSSC performance with the $Cu_{1.8}Se$ and PbSe CEs mainly stemmed from the significantly improved J_{sc} and FF, the enhanced V_{oc} contributed to the better power conversion efficiency in the case of QDSSC equipped with the PbSe CE. The enhanced V_{oc} may be attributed to the tandem effect of the PbSe CE. A recent report by Teng and co-workers demonstrated that PbS, a p-type semiconductor, can serve as a photocathode as well as a CE for QDSSCs, thus being capable of increasing V_{oc}.[31] This observation was affirmed in our study by examining the performance of a QDSSC equipped with PbS CE, whose V_{oc} was the same as the V_{oc} of QDSSC with the PbSe CE (SI Figure S13). We speculate that PbSe, one of the Pb-based chalcogenide family, may exhibit a similar effect as that of PbS.

The electrochemical stability of the CEs with the polysulfide electrolyte was examined by Tafel polarization curve and EIS measurements. Figure 6A and B shows the Tafel polarization curves of the fresh and aged dummy cells composed of $Cu_{1.8}Se$, and PbSe electrodes, respectively. While $Cu_{1.8}Se$ displayed an almost negligible change in the Tafel curves, PbSe showed a gradual decrease in i_0 over time, suggesting that PbSe is unstable when in contact with the polysulfide electrolyte, unlike $Cu_{1.8}Se$. The EIS measurement shown in Figure 6C also confirmed this observation, where no noticeable changes in the EIS parameters were observed for $Cu_{1.8}Se$, whereas R_2 and R_3 became larger for PbSe after 5 h (Table 3). We speculate that the instability of PbSe may be associated with the presence of PbO on the surface of PbSe CE. The dissolution of PbO in basic solutions (for example, aqueous NaOH or KOH solution) has been known as a fast, effective way of removing the oxide

Table 2. EIS Parameters of Pt, $Cu_{1.8}Se$, and PbSe CEs

counter electrode	R_1 (Ω)	R_2 (Ω)	CPE_2 (F)	α_2	R_3 (Ω)	CPE_3 (F)	α_3
Pt	14.9	0.38	1.55×10^{-9}	0.57	7464	1.12×10^{-5}	0.92
$Cu_{18}Se$	12.0	2.39	6.01×10^{-6}	0.89	13.4	2.30×10^{-3}	0.58
PbSe	15.2	6.28	3.38×10^{-6}	0.59	36.3	5.74×10^{-5}	0.86

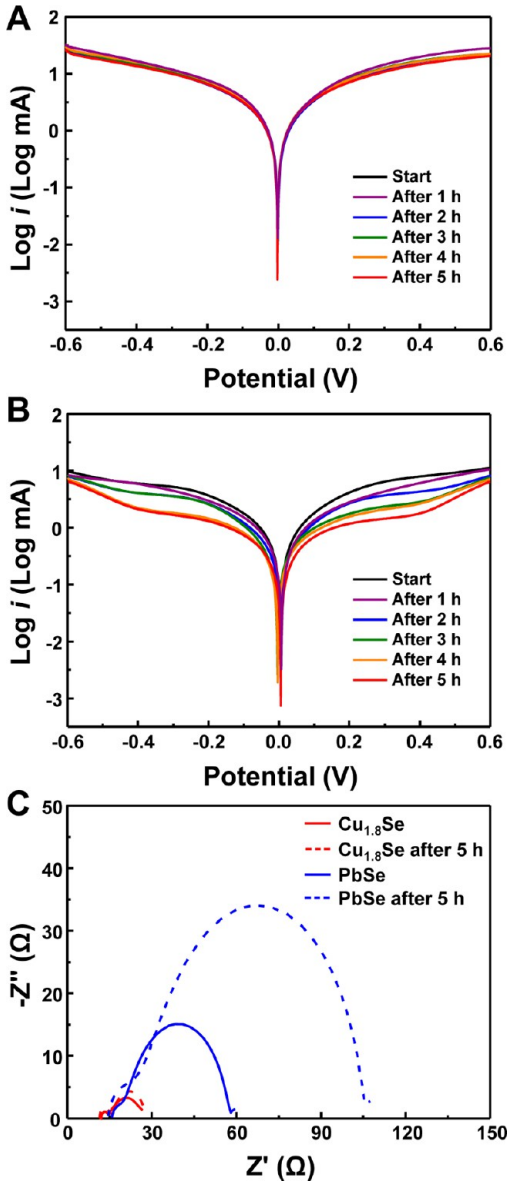

Figure 6. Tafel polarization curves of (A) $Cu_{1.8}Se$ and (B) PbSe electrodes over time and (C) EIS spectra of Pt, $Cu_{1.8}Se$, and PbSe electrodes.

layer from PbSe films.[39] Since the polysulfide electrolyte we used contained an aqueous NaOH solution, the PbO that formed on the surface of the PbSe CE was likely to dissolve off of the surface over time. Given that our cells were not 100% completely sealed against the diffusion of air into the cells, we presume that the fresh PbSe formed after the PbO was dissolved away became reoxidized and the PbO dissolution repeated. This hypothesis is partly supported by the EDS analysis of $Cu_{1.8}Se$ and PbSe electrodes before and after polysulfide exposure (SI Figure S14). There was no significant diminution in the Cu and Se peaks for the $Cu_{1.8}Se$ electrode; however, a dramatic decrease in the Se peak for the PbSe electrode was noticed (note that there was no remarkable change in the Pb peak because the peak from Pb overlaps with that from S), which may be related to the gradual loss of PbSe. Currently, further investigation is underway to elucidate the instability of the PbSe CE.

As the crystallinity, grain size, and composition of electrocatalysts may affect the electrocatalytic activity, we further investigated the effect of these parameters on the electrocatalytic activity of the $Cu_{1.8}Se$ CE. Given that the physicochemical properties of metal chalcogenides are subtly dictated by their stoichiometry, we speculate that the composition, in particular, may become an important factor in governing the electrocatalytic activity. In the case of copper selenides, there exist several stoichiometric and nonstoichiometric compounds.[36] Therefore, the variation in composition may have a profound influence on the electrocatalytic activity of copper selenide. However, it was found that composition tuning seemed to be difficult to achieve by SILAR because only $Cu_{1.8}Se$ film was repeatedly obtained regardless of the concentrations of precursors. The extent of disorder (i.e., crystallinity) and grain size of $Cu_{1.8}Se$ may also affect its electrocatalytic activity. The degree of crystallinity and grain size are in general intimately related to reaction conditions such as temperature and pressure. However, given that SILAR was carried out under ambient condition (i.e., room temperature and pressure), it would be difficult to control crystallinity and grain size. The number of SILAR cycles was likely to be the only reaction parameter that may control these structural properties, and we thus examined their variation as a function of SILAR cycles by XRD analysis. SI Figure S15 shows that as the SILAR cycles increased, the relative intensity of the (220) peak became higher, which stems from the improved crystallinity or from the increase in film thickness. To determine the reason, we performed additional analysis. SEM images of the $Cu_{1.8}Se$ films with different SILAR cycles revealed that the films became thicker and more covered with nanoflakes (SI Figure S16). In addition, the average grain sizes of these $Cu_{1.8}Se$ films, calculated from the (220) peak broadening using the Debye-Scherrer equation, were found to be almost identical, ~13 nm. These observations led us to a conclusion that the increase in the relative intensity of the (220) peak mainly originated from the increase in the film thickness. The electrocatalytic activity of the $Cu_{1.8}Se$ electrode as a function of SILAR cycles was investigated by Tafel and EIS measurements (SI Figure S17 and Table S4). Like the PbSe electrode, the electrocatalytic activity of the $Cu_{1.8}Se$ electrode gradually enhanced over the SILAR cycles. We attributed this increase to a larger active surface area and an improved connection between $Cu_{1.8}Se$ nanoflakes, because there was no significant difference in the crystallinity and grain size of the $Cu_{1.8}Se$ films prepared by SILAR. However, the structural characteristics (that is, crystallinity, grain size, and composition) can be

Table 3. EIS Parameters of $Cu_{1.8}Se$ and PbSe CEs Before and After Exposure to Polysulfide Electrolyte

counter electrode	R_1 (Ω)	R_2 (Ω)	CPE_2 (F)	α_2	R_3 (Ω)	CPE_3 (F)	α_3
$Cu_{18}Se$ (start)	12.0	2.39	6.01×10^{-6}	0.89	13.4	2.30×10^{-3}	0.58
$Cu_{18}Se$ (after 5 h)	11.5	3.60	3.06×10^{-5}	0.97	13.8	1.71×10^{-3}	0.69
PbSe (start)	15.2	6.28	3.38×10^{-6}	0.59	36.3	5.74×10^{-5}	0.86
PbSe (after 5 h)	14.3	12.40	2.68×10^{-6}	0.80	81.1	4.41×10^{-5}	0.87

dx.doi.org/10.1021/am404355m | ACS Appl. Mater. Interfaces 2014, 6, 2335−2343

controlled in other synthesis methods, a delicate control over these parameters may further improve the electrocatalytic activity of the $Cu_{1.8}Se$ electrode, which is the focus of our ongoing research.

The $Cu_{1.8}Se$ CE was compared with the Cu_2S CE, the most common electrocatalyst for highly efficient QDSSCs. Figure 7

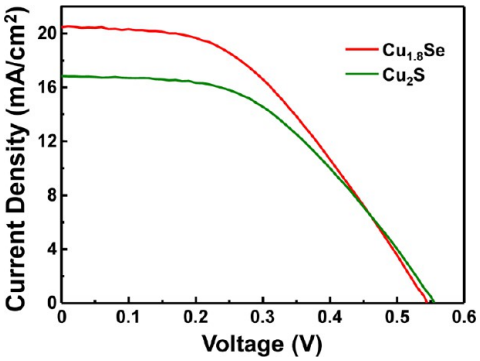

Figure 7. $J-V$ curves of QDSSCs with $Cu_{1.8}Se$ and Cu_2S CEs under 1 SUN (air mass 1.5 G) illumination.

displays the $J-V$ curves of QDSSCs fabricated with the $Cu_{1.8}Se$ and Cu_2S CEs, demonstrating that the QDSSC with the $Cu_{1.8}Se$ CE exhibited a better performance than that with the Cu_2S CE. Since the V_{oc} and FF of both solar cells were nearly identical, this improvement observed with the $Cu_{1.8}Se$ CE mainly stemmed from the increase in J_{sc}, which reflects the superior electrocatalytic activity of the $Cu_{1.8}Se$ CE. The electrocatalytic activity of the $Cu_{1.8}Se$ and Cu_2S CEs toward the polysulfide reduction was investigated by current density-overpotential and EIS measurements (SI Figure S18 and Table S5). The higher current density and lower internal resistance were observed for the $Cu_{1.8}Se$ electrode, which is good accordance with the solar cell performance results.

4. CONCLUSIONS

In summary, we demonstrated the utilization of metal selenides as CE materials for QDSSCs. To the best of our knowledge, this study is the first report of a highly efficient electrocatalyst based on binary metal selenides for polysulfide reduction. The fabrication of various metal selenide CEs was carried out by a fast, reproducible SILAR method, and we found that the $Cu_{1.8}Se$ and PbSe CEs were particularly superior to the Pt CE. The spectroscopic analyses combined with electrochemical measurements revealed that, while both CEs are highly active electrocatalysts, the use of PbSe is limited because of its instability with the polysulfide electrolyte. The newly discovered $Cu_{1.8}Se$ CE was found to perform even better than its traditional competitor, the Cu_2S CE, in QDSSCs. Our discovery of a novel electrocatalyst for the CE of QDSSCs may open a new avenue for the development of highly efficient QDSSCs. We speculate that the search for highly active electrocatalysts can be further extended into other binary selenides and even into ternary and quaternary selenide compounds. Given that the stability of metal selenide compounds against oxidation is in general relatively poor as compared to that of sulfide counterparts, this present study also suggests that a synthesis strategy to prevent the surface oxidation should be developed for the exploration of metal selenide-based electrocatalysts.

■ ASSOCIATED CONTENT

Supporting Information

Characterization of $CdSe/CdS/TiO_2$ film; optimization study on PbSe films via SILAR; Tafel polarization curves and EIS study results of various metal selenide CEs; XPS survey spectra of $Cu_{1.8}Se$ and PbSe films; SEM cross-section images of $Cu_{1.8}Se$, PbSe, and Pt films; EIS spectrum of the Pt counter electrode; $J-V$ curves of QDSSCs with Pt, PbSe, and PbS CEs; SEM-EDS analysis of the $Cu_{1.8}Se$ and PbSe electrodes before and after polysulfide exposure; XRD and SEM analysis of $Cu_{1.8}Se$ films as a function of SILAR cycles and Tafel polarization curves and EIS study results of the films; and current density−overpotential responses and EIS spectra of $Cu_{1.8}Se$ and Cu_2S electrodes. This material is available free of charge via the Internet at http://pubs.acs.org.

■ AUTHOR INFORMATION

Corresponding Author

*E-mail: jbang@hanyang.ac.kr.

Author Contributions

H.M.C. and I.A.J. contributed equally to this work.

Notes

The authors declare no competing financial interest.

■ ACKNOWLEDGMENTS

This research was supported by a grant from the Basic Science Research Program through the National Research Foundation of Korea (NRF) funded by the Ministry of Science, ICT and Future Planning (No. NRF-2013R1A1A1008762), and by a grant from the Human Resources Development Program (No. 20124030200130) of the Korea Institute of Energy Technology Evaluation and Planning (KETEP) funded by the Ministry of Trade, Industry and Energy.

■ REFERENCES

(1) Kamat, P. V. Boosting the Efficiency of Quantum Dot Sensitized Solar Cells through Modulation of Interfacial Charge Transfer. *Acc. Chem. Res.* **2012**, *45*, 1906−1915.

(2) Bang, J. H.; Kamat, P. V. Quantum Dot Sensitized Solar Cells. A Tale of Two Semiconductor Nanocrystals: CdSe and CdTe. *ACS Nano* **2009**, *3*, 1467−1476.

(3) Lee, H.; Wang, M.; Chen, P.; Gamelin, D. R.; Zakeeruddin, S. M.; Grätzel, M.; Nazeeruddin, M. K. Efficient CdSe Quantum Dot-Sensitized Solar Cells Prepared by an Improved Successive Ionic Layer Adsorption and Reaction Process. *Nano Lett.* **2009**, *9*, 4221−4227.

(4) Lee, Y.-L.; Lo, Y.-S. Highly Efficient Quantum-Dot-Sensitized Solar Cell Based on Co-Sensitization of CdS/CdSe. *Adv. Funct. Mater.* **2009**, *19*, 604−609.

(5) Shalom, M.; Buhbut, S.; Tirosh, S.; Zaban, A. Design Rules for High-Efficiency Quantum-Dot-Sensitized Solar Cells: A Multilayer Approach. *J. Phys. Chem. Lett.* **2012**, *3*, 2436−2441.

(6) Bang, J. H.; Kamat, P. V. Solar Cells by Design: Photoelectrochemistry of TiO_2 Nanorod Arrays Decorated with CdSe. *Adv. Funct. Mater.* **2010**, *20*, 1970−1976.

(7) Yu, X.-Y.; Liao, J.-Y.; Qiu, K.-Q.; Kuang, D.-B.; Su, C.-Y. Dynamic Study of Highly Efficient CdS/CdSe Quantum Dot-Sensitized Solar Cells Fabricated by Electrodeposition. *ACS Nano* **2011**, *5*, 9494−9500.

(8) Zhang, J.; Tang, C.; Bang, J. H. $CdS/TiO_2-SrTiO_3$ Heterostructure Nanotube Arrays for Improved Solar Energy Conversion Efficiency. *Electrochem. Commun.* **2010**, *12*, 1124−1128.

(9) McDaniel, H.; Fuke, N.; Pietryga, J. M.; Klimov, V. I. Engineered $CuInSe_xS_{2-x}$ Quantum Dots for Sensitized Solar Cells. *J. Phys. Chem. Lett.* **2013**, *4*, 355−361.

(10) Santra, P. K.; Kamat, P. V. Mn-Doped Quantum Dot Sensitized Solar Cells: A Strategy to Boost Efficiency over 5%. *J. Am. Chem. Soc.* **2012**, *134*, 2508−2511.
(11) Li, T.-L.; Lee, Y.-L.; Teng, H. High-Performance Quantum Dot-Sensitized Solar Cells Based on Sensitization with $CuInS_2$ Quantum Dots/CdS Heterostructure. *Energy Environ. Sci.* **2012**, *5*, 5315−5324.
(12) Yan, K.; Zhang, L.; Qiu, J.; Qiu, Y.; Zhu, Z.; Wang, J.; Yang, S. A Quasi-Quantum Well Sensitized Solar Cell with Accelerated Charge Separation and Collection. *J. Am. Chem. Soc.* **2013**, *135*, 9531−9539.
(13) Chang, J.-Y.; Su, L.-F.; Li, C.-H.; Chang, C.-C.; Lin, J.-M. Efficient "Green" Quantum Dot-Sensitized Solar Cells Based on Cu_2S−$CuInS_2$−ZnSe Architecture. *Chem. Commun.* **2012**, *48*, 4848−4850.
(14) Pan, Z.; Zhao, K.; Wang, J.; Zhang, H.; Feng, Y.; Zhong, X. Near Infrared Absorption of $CdSe_xTe_{1-x}$ Alloyed Quantum Dot Sensitized Solar Cells with More than 6% Efficiency and High Stability. *ACS Nano* **2013**, *7*, 5215−5222.
(15) Lee, J.-W.; Son, D.-Y.; Ahn, T. K.; Shin, H.-W.; Kim, I. Y.; Hwang, S.-J.; Ko, M. J.; Sul, S.; Han, H.; Park, N.-G. Quantum-Dot-Sensitized Solar Cell with Unprecedentedly High Photocurrent. *Sci. Rep.* **2013**, *3*, 1050.
(16) Sixto, G.; Iván, M.-S.; Lorena, M.; Nestor, G.; Teresa, L.-V.; Roberto, G.; Lina, J. D.; Qing, S.; Taro, T.; Juan, B. Improving the Performance of Colloidal Quantum-Dot-Sensitized Solar Cells. *Nanotechnology* **2009**, *20*, 295204.
(17) Hodes, G.; Manassen, J.; Cahen, D. Electrocatalytic Electrodes for the Polysulfide Redox System. *J. Electrochem. Soc.* **1980**, *127*, 544−549.
(18) Radich, J. G.; Dwyer, R.; Kamat, P. V. Cu_2S Reduced Graphene Oxide Composite for High-Efficiency Quantum Dot Solar Cells. Overcoming the Redox Limitations of S^{2-}/S_n^{2-} at the Counter Electrode. *J. Phys. Chem. Lett.* **2011**, *2*, 2453−2460.
(19) Yang, Z.; Chen, C.-Y.; Liu, C.-W.; Chang, H.-T. Electrocatalytic Sulfur Electrodes for CdS/CdSe Quantum Dot-Sensitized Solar Cells. *Chem. Commun.* **2010**, *46*, 5485−5487.
(20) Tachan, Z.; Shalom, M.; Hod, I.; Rühle, S.; Tirosh, S.; Zaban, A. PbS as a Highly Catalytic Counter Electrode for Polysulfide-Based Quantum Dot Solar Cells. *J. Phys. Chem. C* **2011**, *115*, 6162−6166.
(21) Yang, Y.; Zhu, L.; Sun, H.; Huang, X.; Luo, Y.; Li, D.; Meng, Q. Composite Counter Electrode Based on Nanoparticulate PbS and Carbon Black: Towards Quantum Dot-Sensitized Solar Cells with Both High Efficiency and Stability. *ACS Appl. Mater. Interfaces* **2012**, *4*, 6162−6168.
(22) Xu, J.; Yang, X.; Wong, T.-L.; Lee, C.-S. Large-Scale Synthesis of Cu_2SnS_3 and $Cu_{1.8}S$ Hierarchical Microspheres as Efficient Counter Electrode Materials for Quantum Dot Sensitized Solar Cells. *Nanoscale* **2012**, *4*, 6537−6542.
(23) Yang, Z.; Chen, C.-Y.; Liu, C.-W.; Li, C.-L.; Chang, H.-T. Quantum Dot−Sensitized Solar Cells Featuring CuS/CoS Electrodes Provide 4.1% Efficiency. *Adv. Energy Mater.* **2011**, *1*, 259−264.
(24) Faber, M. S.; Park, K.; Cabán-Acevedo, M.; Santra, P. K.; Jin, S. Earth-Abundant Cobalt Pyrite (CoS_2) Thin Film on Glass as a Robust, High-Performance Counter Electrode for Quantum Dot-Sensitized Solar Cells. *J. Phys. Chem. Lett.* **2013**, *4*, 1843−1849.
(25) Zhang, X.; Huang, X.; Yang, Y.; Wang, S.; Gong, Y.; Luo, Y.; Li, D.; Meng, Q. Investigation on New $CuInS_2$/Carbon Composite Counter Electrodes for CdS/CdSe Cosensitized Solar Cells. *ACS Appl. Mater. Interfaces* **2013**, *5*, 5954−5960.
(26) Xu, J.; Yang, X.; Yang, Q.-D.; Wong, T.-L.; Lee, C.-S. Cu_2ZnSnS_4 Hierarchical Microspheres as an Effective Counter Electrode Material for Quantum Dot Sensitized Solar Cells. *J. Phys. Chem. C* **2012**, *116*, 19718−19723.
(27) Cao, Y.; Xiao, Y.; Jung, J.-Y.; Um, H.-D.; Jee, S.-W.; Choi, H. M.; Bang, J. H.; Lee, J.-H. Highly Electrocatalytic $Cu_2ZnSn(S_{1-x}Se_x)_4$ Counter Electrodes for Quantum-Dot-Sensitized Solar Cells. *ACS Appl. Mater. Interfaces* **2013**, *5*, 479−484.
(28) Zeng, X.; Xiong, D.; Zhang, W.; Ming, L.; Xu, Z.; Huang, Z.; Wang, M.; Chen, W.; Cheng, Y.-B. Spray Deposition of Water-Soluble Multiwall Carbon Nanotube and $Cu_2ZnSnSe_4$ Nanoparticle Composites as Highly Efficient Counter Electrodes in A Quantum Dot-Sensitized Solar Cell System. *Nanoscale* **2013**, *5*, 6992−6998.
(29) Sarkar, S. K.; Kababya, S.; Vega, S.; Cohen, H.; Woicik, J. C.; Frenkel, A. I.; Hodes, G. Effects of Solution pH and Surface Chemistry on the Postdeposition Growth of Chemical Bath Deposited PbSe Nanocrystalline Films. *Chem. Mater.* **2007**, *19*, 879−888.
(30) Chen, H.; Zhu, L.; Liu, H.; Li, W. ITO Porous Film-Supported Metal Sulfide Counter Electrodes for High-Performance Quantum-Dot-Sensitized Solar Cells. *J. Phys. Chem. C* **2013**, *117*, 3739−3746.
(31) Lin, C.-Y.; Teng, C.-Y.; Li, T.-L.; Lee, Y.-L.; Teng, H. Photoactive p-Type PbS as a Counter Electrode for Quantum Dot-Sensitized Solar Cells. *J. Mater. Chem. A* **2013**, *1*, 1155−1162.
(32) Hodes, G. Photoelectrochemical Cell Measurements: Getting the Basics Right. *J. Phys. Chem. Lett.* **2012**, *3*, 1208−1213.
(33) Duay, J.; Sherrill, S. A.; Gui, Z.; Gillette, E.; Lee, S. B. Self-Limiting Electrodeposition of Hierarchical MnO_2 and $M(OH)_2/MnO_2$ Nanofibril/Nanowires: Mechanism and Supercapacitor Properties. *ACS Nano* **2013**, *7*, 1200−1214.
(34) Xue, C.; Papadimitriou, D.; Raptis, Y. S.; Richter, W.; Esser, N.; Siebentritt, S.; Lux-Steiner, M. C. Micro-Raman Study of Orientation Effects of Cu_xSe-Crystallites on Cu-rich $CuGaSe_2$ Thin Films. *J. Appl. Phys.* **2004**, *96*, 1963−1966.
(35) Romano-Trujillo, R.; Rosendo, E.; Ortega, M.; Morales-Sánchez, A.; Gracia, J. M.; Díaz, T.; Nieto, G.; García, G.; Luna-López, J. A.; Pacio, M. Synthesis and Characterization of PbSe Nanoparticles Obtained by A Colloidal Route Using Extran as A Surfactant at Low Temperature. *Nanotechnology* **2012**, *23*, 185602.
(36) Riha, S. C.; Johnson, D. C.; Prieto, A. L. Cu_2Se Nanoparticles with Tunable Electronic Properties Because of a Controlled Solid-State Phase Transition Driven by Copper Oxidation and Cationic Conduction. *J. Am. Chem. Soc.* **2010**, *133*, 1383−1390.
(37) Hauch, A.; Georg, A. Diffusion in The Electrolyte and Charge-Transfer Reaction at The Platinum Electrode in Dye-Sensitized Solar Cells. *Electrochim. Acta* **2001**, *46*, 3457−3466.
(38) Murakami, T. N.; Ito, S.; Wang, Q.; Nazeeruddin, M. K.; Bessho, T.; Cesar, I.; Liska, P.; Humphry-Baker, R.; Comte, P.; Péchy, P.; Grätzel, M. Highly Efficient Dye-Sensitized Solar Cells Based on Carbon Black Counter Electrodes. *J. Electrochem. Soc.* **2006**, *153*, A2255−A2261.
(39) Gautier, C.; Cambon-Muller, M.; Averous, M. Study of PbSe Layer Oxidation and Oxide Dissolution. *Appl. Sur. Sci.* **1999**, *141*, 157−163.